A physics-based modeling framework to assess the cost scaling of additive manufacturing, with application to laser powder bed fusion

Kaitlyn Gee, Suh In Kim, Haden Quinlan, A. John Hart
Department of Mechanical Engineering, Massachusetts Institute of Technology, Cambridge, MA, 02139, USA

Structured abstract

Purpose - We present a framework to estimate throughput and cost of additive manufacturing (AM) as related to process parameters, material thermodynamic properties, and machine specifications. Taking a 3D model of the part design as direct input, the model uses a parametrization of the rate-limiting physics of the AM build process—herein focusing on laser powder bed fusion (LPBF) and scaling of melt pool geometry —to estimate part- and material-specific build time. From this estimate, per-part cost is calculated using a quantity-dependent activity-based production model.

Design/methodology/approach - Analysis tools that assess how design variables and process parameters influence production cost increase our understanding of the economics of AM, thereby supporting its practical adoption. To this aim, our framework produces a representative scaling among process parameters, build rate, and production cost.

Findings - For exemplary alloys and LPBF systems, predictions reveal the underlying tradeoff between production cost and machine capability, and look beyond the capability of currently commercially available equipment. As a proxy for build quality, the number of times each point in the build is re-melted is derived analytically as a function of process parameters, showcasing the tradeoff between print quality due to increased melting cycles, and throughput.

Originality/value - For exemplary alloys and LPBF systems, predictions reveal the underlying tradeoff between production cost and machine capability, and look beyond the capability of currently commercially available equipment. As a proxy for build quality, the number of times each point in the build is re-melted is derived analytically as a function of process parameters, showcasing the tradeoff between print quality due to increased melting cycles, and throughput.

Keywords: additive manufacturing, laser powder bed fusion, cost estimation, process parameters, productivity

Plain language summary: The rate and cost of additive manufacturing varies widely depending on which part, material, machine, and set of process parameters are chosen. Our analysis tools show how these variables affect build throughput and production cost, herein for laser-based metal 3D printing.

1 INTRODUCTION

The tradeoffs among design, manufacturability, and cost for additive manufacturing (AM) are difficult to assess, especially at the early stage of ideation and product development.

Each AM process has its own overall design constraints, such as the requirement for support structures (Kranz *et al.*, 2014) or the density of packing parts in two- or three-dimensions (Oh *et al.*, 2018). Designers must also address the myriad implications of part geometry, build configuration, and/or material selection (Cheng and To, 2019). In order to accurately estimate AM cost and to bound the practical design space, it is critical for us to understand how these factors are interrelated in addition to the intrinsic process physics and machine specifications.

Among a growing portfolio of AM processes, laser powder bed fusion (LPBF) of metals can fabricate highly complex components and is compatible with many conventional and specialty alloys. Qualified commercial applications of LPBF include jet engine nozzles (James, 2021), components of hip implants, cutting tools with enhanced performance, and bespoke decorative fixtures. While LPBF and many other AM processes are still largely limited to high-value applications that can tolerate costly and lengthy qualification, wider use of LPBF requires tight integration of design capabilities, manufacturability constraints, and cost analysis. In this study, we focus on two metrics of AM capability that determine its utility: throughput (i.e. volumetric build rate) and production cost.

As with LPBF, the throughput of an AM process—i.e., the build rate achieved by the associated equipment—is a primary determinant of its overall productivity, and the ultimate component cost. Therefore, understanding the factors influencing throughput is key to early-stage design guidance, and to evaluating potential business cases and strategies for adoption of AM. Build time estimations can be general, i.e., reflecting an approximate rate for a process or machine, or tailored to a specific component based on the 3D CAD file. Early examples in the literature are found for stereolithography (Chen and Sullivan, 1996; Giannatsis *et al.*, 1999), selective laser sintering (Choi and Samavedam, 2002), electron beam melting (Baumers *et al.*, 2016), and laminated object manufacturing (Kechagias *et al.*, 2004), among others. For stereolithography, rate models are commonly built off the Beer-Lambert law of absorption to characterize the photopolymerization of resin (Jacobs, 1993), but rate estimation for LPBF involves a more complex coupling among process physics, build rate and part quality (Meier *et al.*, 2018; Mukherjee *et al.*, 2018). For LPBF, a key determinant of rate is the relationship between process parameters (e.g., laser power, spot size, scanning speed, layer thickness), melt pool geometry, and process instabilities such as keyholing or lack of fusion (Cunningham *et al.*, 2019; Gusarov and Smurov, 2010; King *et al.*, 2014; Rubenchik *et al.*, 2018; Thomas *et al.*, 2016). The correlation between processing parameters and achievement of full-density parts with LPBF is often performed by a parametric study of laser power and scan speed while holding other parameters constant (e.g., layer thickness, material, and powder size). Empirical studies have shown that the microstructure evolution and mechanical properties of LPBF-produced metals are strongly correlated to the printing process parameters (KOTADIA, 2021; Kruth *et al.*, 2004; Nath *et al.*, 2021; Yadroitsev *et al.*, 2007). Therefore, such correlations can be valuable input to models that evaluate tradeoffs between cost and component quality, via considering how process parameters influence both build rate and desired properties and/or the formation of defects during AM.

Accurate cost estimation is essential to assess viable business cases for AM. In order to accurately relate process performance to AM economics, cost estimation should be based in the fundamental limits of the process physics, despite the fact that the underlying dynamics of LPBF process stability are difficult to quantify accurately (Oliveira *et al.*, 2020). AM cost modeling has most commonly adopted activity-based methods (Alexander *et al.*, 1998; Costabile *et al.*, 2017), wherein cost is decomposed into constituent direct and indirect components, and time estimates of the build process itself informs the net production cost per unit. The main drivers for cost are machine and material expenses (Lindemann *et al.*, 2012; Thomas *et al.*, 2016). Moreover, while the cost advantages of AM for small-volume, and/or customized products are well-documented (Awad *et al.*, 2018; Tofail *et al.*, 2018; Tuck *et al.*, 2008; Weller *et al.*, 2015), the relationship between production quantity and unit cost requires careful implementation of activity-based models along with consideration of the part- and process-dependent throughput, among many other factors (Ding *et al.*, 2021). Most commonly and conveniently, a constant build rate is assumed due to the intricacies of rate estimation or lack of available empirical data (Lindemann *et al.*, 2012). Estimates of cost are therefore most easily based on nominal build rate estimates that capture the bulk volumetric print rate of a particular AM machine which has been parameter-optimized to a specific material and quality output. In this sense, our current understanding of AM cost is constrained to the machine and process capability of currently existing AM systems. As such, it is challenging to obtain a parametric understanding of how AM process parameters relate to cost, and how tradeoffs between throughput and machine capability

The goals of this study are first to explore the influence of process parameter selection on overall build rate for LPBF. Integrating digital mesh processing, scaling laws of melt pool geometry, and representative approximations of laser scan strategy, we construct a parametrized model of the rate-limiting physics of LPBF to estimate part-specific build time. Second, we interrogate the relationship between build rate and cost over a range of commercial machines and materials, enabling parametric analysis of tradeoffs among resolution, throughput, and cost. Finally, we extrapolate these models to forecast the cost effectiveness of LPBF beyond the capabilities of current AM systems.

2 METHODS

We developed a purpose-built numerical pipeline to enable end-to-end parametric build rate and cost analysis. An overview of the coupled digital file analysis and physics-based process modeling is shown in Figure 1, depicting parallel workflows for digital geometry processing and physical melt pool scaling. This pipeline couples process and materials data to established physical models for LPBF. Code was developed in-house using the Julia scientific programming language.

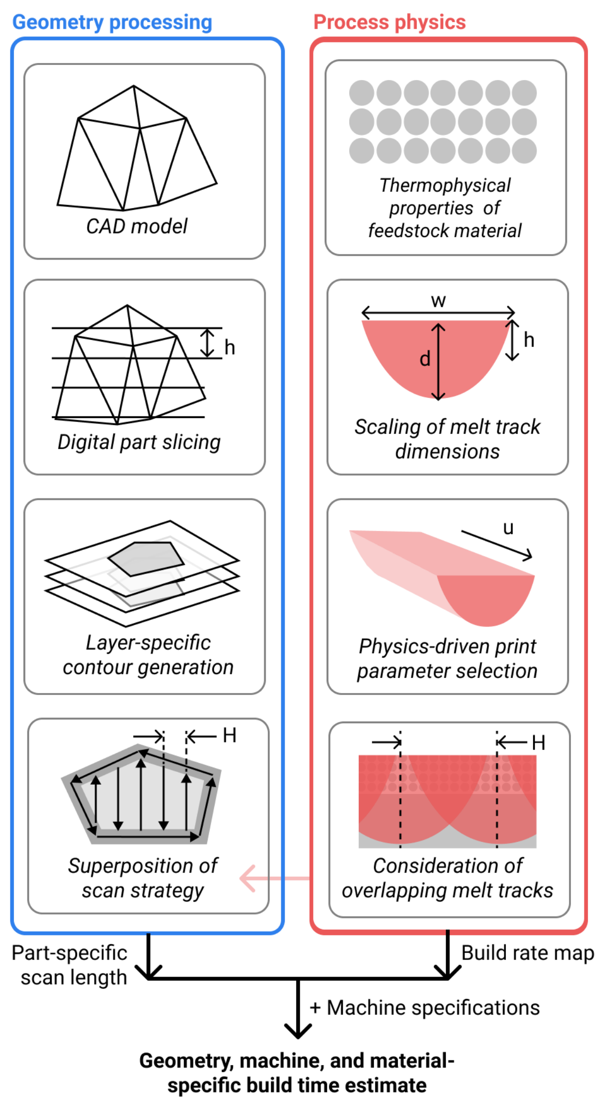

Figure 1. Graphics processing workflow for the physics-based LPBF rate model, which performs part slicing and calculates a part-specific print length as a proxy for the laser toolpath. Model inputs are: a digital part file, machine specifications (such as laser power, laser spot size, and build chamber volume, Table 3), and thermophysical properties of the feedstock metal powder (Table 1). The geometry processing workflow digitally slices the part file based on a specified layer height *h*, and generates closed-loop contours bounding the area to be printed on

each layer. After superimposing a representative scan strategy, an estimate of the total linear length of scanning and number of recoating layers is produced. The process physics uses empirically determined scaling laws between laser and material inputs to estimate the desired scan speed *u* to produce a melt track of depth *d* and width *w*. Accounting for the overlap of melt tracks both horizontally (i.e. adjacent, in-layer) and vertically, this workflow combines the geometry processing outputs to yield total build time specific to part geometry, machine specification, and material properties.

2.1 Melt pool scaling model

Estimation of process throughput (i.e. volumetric build rate) is predicated on the underlying physics of the rate-limiting step in the process. For LPBF, the volumetric rate at which the feedstock powder can be transformed into an ultimately solidified melt track is the core element, subject to the required input energy to melt the powder. For a user-selected laser power, laser spot size (i.e. Gaussian beam half-width), feedstock material, layer height and desired melt pool depth, our code computes the appropriate laser scan speed and hatch spacing

We configure our code such that the model of melt pool-laser dynamics requires the following user inputs: (1) laser power, (2) laser spot size (i.e. Gaussian beam half-width), (3) absorptivity of the laser by the build surface, (4) layer height, and (5) desired melt pool depth. The melt pool depth is parametrized by the ratio of the melt pool depth to the printed layer height, herein termed overmelt ϕ. The printed layer height in the model represents the thickness of the solidified, fully dense layer. Definition of melt track parameters are shown in Figure 2.

For melt pool depth (i.e. the solidified depth of the melt track), we adopt the scaling proposed by Ye et al, which was determined experimentally using in situ optical absorptivity measurements coupled to a hydrodynamic finite element model (Ye *et al.*, 2019). From Ye et al, the laser scan speed is calculated as:

$$u = \frac{KAP}{\pi H_m a d}$$

where u is laser scan velocity, K is a empirically-determined geometrical factor that accounts for the differences between actual melt pool geometry and the simplified model, A is the minimal material absorptivity, P is laser power (W), H_m is the volumetric melting enthalpy (J/m^3), a is laser beam radius (μm), and d is the depth of the melt pool (μm).

For melt pool width, we employ the scaling law of Groβmann et al (Großmann *et al.*, 2019), which was derived using dimensional analysis in conjunction with an averaged energy balance, and validated with empirical data.

$$w = C\sqrt{\frac{P}{u}}\sqrt{\frac{1}{\rho C_p \Delta T_l}}$$

where w is the width of the melt track (i.e., perpendicular to the scan direction), C is a material-specific proportionality constant, P is laser power, u is laser scanning speed, ρ is density, C_p is specific heat capacity, and ΔT_l is the change in temperature between the initial and liquid state of powder. For the following results, ΔT_l is set to $T_m - T_{amb}$, where T_{amb} is the ambient temperature of the build chamber and assumed to be 100 deg C. The parameter C is equivalent to $\sqrt{\alpha/\varepsilon}$ where α relates to the material's absorptivity and ε is a geometry factor describing the shape of the melt pool. Values of C were determined using calculations of the non-linear geometry factor ε followed by regression analysis to yield C (Großmann *et al.*, 2019).

	ρ	T_m	C_p	D*	C (Großmann *et al.*, 2019)	H_m	K (Großmann *et al.*, 2019)	A_m (Ye *et al.*, 2019)
	g/cc	K	J/kg-K	m^2/s	-	kJ/cm^3	-	-
AlSi10Mg	2.67	870	910	4.90e-5	0.49	2.11	0.6	0.18
Ti6Al4V	4.41	1933	526.3	2.85e-6	0.64	4.48	0.6	0.26
1.2709 Steel	8.05	1445	450	4.86e-6	0.48	5.23	0.6	0.28

Table 1. Material-specific inputs for selected alloys. T_m is the desired melting temperature, C_p is specific heat, C is an empirically determined scaling constant, H_m is the enthalpy of fusion, and A_m is the absorptivity between the metal powder and laser. *While thermal diffusivity D is not necessary for the computation of laser scan speed and melt track width, it is required for calculation of normalized enthalpy in later sections.

These scaling laws provide accurate, straightforward approximations of the scaling between laser control parameters, material properties and melt track dimensions, as validated by empirical data. As analytical and explicit equations, these functions can be implemented in our larger computational workflow. The modular structure of our approach is such that alternate models can be incorporated as desired. For instance, our use of two independent scaling models for melt pool width and depth can be replaced by a single (albeit more computationally intensive) numerical model for the melt pool dynamics in future work, from which the melt pool dimensions or the full shape can be extracted for further analysis.

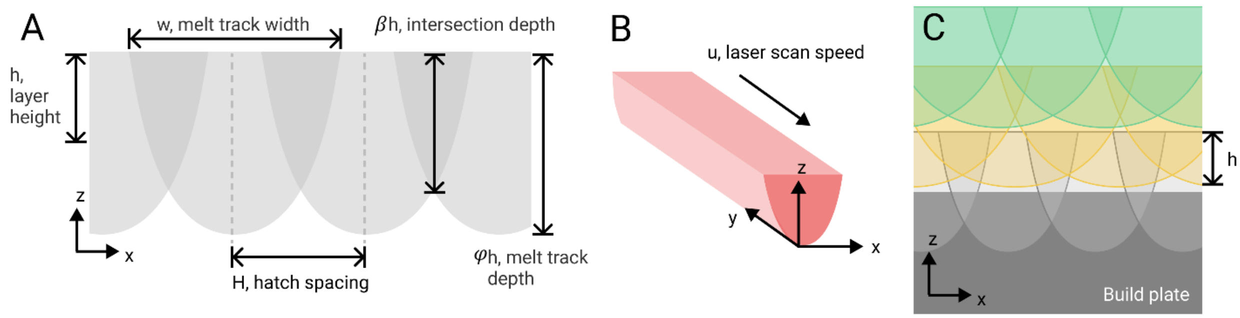

Figure 2. Definition of melt track parameters for physics-based LPBF rate model. (A) Cross-section of overlapping melt tracks, orthogonal to build direction. (B) Parabolic melt track. (C) Cross-section of multiple print layers, showing the assumed vertical and lateral overlap. Laser scan direction is rotated by 120 deg between print layers.

2.2 Geometry processing

Three-dimensional models of components for build rate and cost analysis are imported as .STL files using the FileIO and MeshIO libraries ("GitHub - JuliaIO/MeshIO.jl: IO for Meshes", 2019). After the file is imported, the following operations are performed: (1) storing the vertices and faces of each triangle, (2) scaling vertices to convert units, (3) extracting bounding box limits, (4) resetting the mesh origin to (0.0, 0.0 ,0.0) in Cartesian coordinates, (5) computing mesh volume (Zhang and Chen, 2001), and (6) computing mesh surface area (i.e. sum of all triangle areas). Key metrics such as mesh volume and surface area become outputs of the processing workflow. An in-house algorithm slices the mesh by computing triangle-plane intersections at each layer height, and generates in-layer contours using a state machine-enabled approach to assign edges to closed loops.

To calculate the build time for each layer of a digital model, as related to LPBF, a simple laser scan strategy is simulated. A single pass around the perimeter of each contour (i.e., skin) and a standard zig-zag scan pattern for the area (i.e., core) is specified for each print layer. The number of contour passes and the core scan parameters can be modified as desired by the user, and especially the contour parameters are known to influence surface roughness and subsurface porosity (Artzt *et al.*, 2020).

For LPBF, hatch spacing (i.e., the in-plane distance between the centerlines of adjacent melt tracks), along with overmelt, determines the number of times each location is re-melted as consecutive tracks and layers are scanned. Our model assumes, disregarding effects from skin-core overlap, that each internal melt track overlaps with two other melt tracks in each layer, i.e. one on the right side and one on the left. Hatch H is bounded as $0 < H \leq w/2$ where w is the width of the melt track. Therefore, the effective melt track width, i.e. the width of printed material from a single pass of the laser is equal to the hatch, i.e. $H = w^*$. Collectively, melt track width, melt track depth, layer height, overmelt and hatch spacing describe the physical dimensions and layout of overlapping melt tracks within the printed part. This is shown in Figure 2A.

Moreover, overlap between the skin and core scan paths is considered, such that the total laser scan length for a given layer is:

$$L_i = \frac{a_i}{w^*} + p_i - \mu w^* p_i$$

where i is the print layer of interest, L_i is the predicted total scan length required, a_i is the total area bounded by all contours in the layer, w^* is the modified width of the melt track (i.e. the additional print width due to the current melt track, not accounting for the overlap between the current and previous melt track) and p_i is the total perimeter of all contours in the layer. We define a μ factor to account for the overlap between the area and perimeter scans; for the following analysis, it is set to 0.8. The total scan length is calculated for each layer:

$$L_{scan} = \sum_{i=1}^{N} \frac{a_i}{w^*} + p_i - \mu w^* p_i$$

where L_{scan} is the total scanning length required to produce the part geometry and N is the total number of layers in the print. Thus, the ultimate output of the geometry processing workflow is L_{scan}, which conceptually translates input part volume into the series and length scale of actions required to produce that volume.

The effective melt track width is used in the geometric processing workflow to output L_{scan}, i.e. the total scan length required to produce the part geometry. Assuming the same scan parameters throughout the print (i.e., no modulation of power or scan speed), the total scanning time is $t_{scan} = L_{scan}/u$. Mechanistically, L_{scan} captures the physical dimensions and layout of melt tracks, is driven by d, w, $H, h,$ overmelt, and material parameters, and considers the nuances of the print process such as scanning of the skin and core separately. Moreover, the determination of u through the scaling model captures the physical laser-material interactions that melt the powder. Together, these variables produce an estimate of total scanning time for a desired geometry. Notably, in this analysis we do not consider the motion dynamics of the galvanometers used to position the laser beam(s), i.e., the time necessary to accelerate and decelerate the scanning mirrors at the beginning and end of each scan segment.

2.3 Build time estimation

The total time required to print t_{print} is the sum of the total time to scan all layers t_{scan}. To determine an effective build rate $\dot{B}$, we divide the input mesh volume V by total print time t_{print}, i.e. $\dot{B} = V/t_{print}$. While the following cost model includes time for inter-layer recoating, machine warm-up, cool-down and build exchange, only the scanning time is represented by the volumetric build rate $\dot{B}$. From the adopted scalings for melt pool width and depth, we compute maps that show the dependence of volumetric build rate on the above listed input parameters, as described in the Results section.

For Figure 4, showing the scaling of $\dot{B}$ with laser power and scan speed, a cube of V =1cc is used. For Figures 5 and 6 showing cost scalings as a function of production quantity, an exemplary bracket geometry is used. The bounding box of the bracket is 7.5 x 1.25 x 5 cm and the material volume of the bracket is 29.1 cc.

2.4 Incorporation of physical build limits

Importantly, this physics-based build rate estimation can run without bound. It accordingly suggests that arbitrarily high combined values of power and scan speed, for the same spot size, will lead to greater build rate. However, it is well known that the energy density applied to the melt pool is limited by the formation of keyhole porosity. Keyholing is widely studied in welding, and can be desired when a deep weld is required (i.e. for joining two materials). The keyhole melt pool shape is deep and narrow. Keyhole pores form as the surface temperature of the melt pool increases, the recoil pressure due to evaporation at the surface forms a depression in the melt pool, and the resulting depression penetrates further into the material. This has been visualized via high-speed X-ray scattering (Cunningham *et al.*, 2019). The dynamics of keyhole formation, and potential means of process control for mitigation, are subjects of ongoing research; nevertheless, we can apply a threshold to the rate map to identify a potential upper-bound on the build rate in LPBF.

We use the parameter normalized enthalpy as an indication of the proximity of the process parameters to a practical build rate limit. Normalized enthalpy $\Delta H/h_s$ is defined as the enthalpy input into powder by the laser, normalized by the enthalpy of the material at its melting temperature (Hann *et al.*, 2011):

$$\frac{\Delta H}{h_s} = \frac{AP}{\pi h_s \sqrt{Dua^3}}$$

where A is laser absorptivity, P is laser power, D is the material's thermal diffusivity, u is the laser scan speed, and a is laser beam diameter. Values of D are shown in Table 1. Normalized enthalpy therefore considers both laser control parameters (i.e., laser power, scan speed, and spot size) and the thermodynamic properties of the feedstock material.

2.5 Activity-based cost modeling

The physics-based LPBF rate model allows us to build a parameterized cost model that reflects (i) the relationship between machine capability (i.e. laser power, laser spot size) and per-part cost, and (ii) the key contributors of cost based on activity within the print sequence. The cost model considers a single part geometry with a total production quantity of N parts. In this model, parts are packed within each virtual build in a single layer, based on simple division of the build area by the in-plane bounding box area of the part defined by the desired print orientation (Figure 3). Yield losses are captured by the assumed uptime of the machine, i.e., uptime denotes all machine utilization time resulting in successful prints. This model only considers the printing cost; post-processing costs including de-powdering, support removal, and heat treatment are not included.

Per-part cost is decomposed into material cost, machine usage cost, consumables cost, and labor cost. Costs are assigned based on the corresponding activities and expenses to each category (Baumers *et al.*, 2016). Thus, the estimated cost per part can be expressed as

$$C_{total} = C_m + C_e + C_c + C_l$$

where Cm, Ce, Cc, and Cl are the costs due to material usage, equipment/machine utilization, consumables, and labor, respectively. As such, this framework is adaptable to include the rate model for any AM process, with application here to LPBF. A detailed description of the activity-based cost model is included in the supporting information.

In brief, the formulation of the cost model for each category of expenses is as follows.

- Material cost has three components: (i) the cost of powder to produce the finished part, (ii) the cost of powder to produce part supports, and (iii) the cost of surrounding powder that cannot be recycled.
- Machine cost considers (i) the capital cost of the printer, (ii) supporting infrastructure requirements, and (iii) yearly maintenance costs. The cost of the machine is discounted by yearly cash flows, from which an hourly utilization cost is derived. Utilization time considers the time for printing (part-dependent, scanning and recoating time) as well as time allocation for printer warm-up, cool-down post-print, and build exchange. Per-layer recoat time is approximated by the time required for the build platform to move vertically, and for the recoating device to travel horizontally, multiplied by the number of layers required to produce the part.
- The build consumables considered by the LPBF model are (i) gas flow used to inert the build chamber before and during printint, (ii) the build plate, and (iii) energy consumption of the machine. While energy consumption may have important implications for the environmental impact of LPBF, we argue that the cost of electricity is negligible in relation to other per-part costs.
- Labor cost accounts for the work required to setup, supervise and exchange builds. We consider the labor associated with the physical build itself, not including the labor costs of part and process design in the product development or qualification phases.

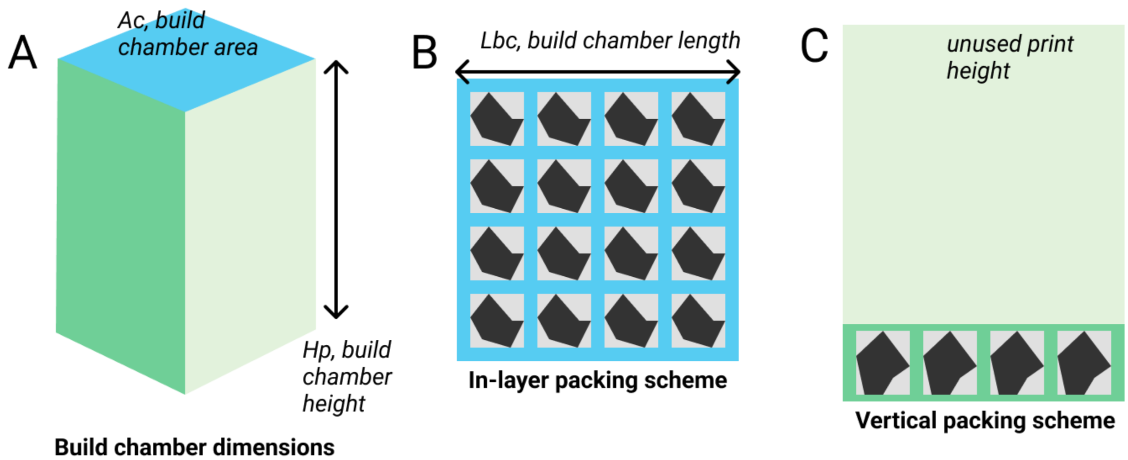

Figure 3. Visualization of simplified packing scheme for the cost model. We consider a rectangular build volume with area A_c and height H_p (left). The in-layer packing scheme considers the ratio of build chamber cross-sectional area to part footprint (center). The grey box denotes the part footprint while the black shape represents actual part geometry. The vertical packing scheme considers the ratio of build chamber height to part height (right). The grey shape denotes the part's bounding box while the black shape represents actual part geometry. we consider only a single layer of parts (as is typical in LPBF) and therefore a portion of the build chamber is unused. We assume powder is filled to the height of the parts to be printed, and therefore the powder surrounding that parts (dark green) remains unfused and is recycled with a small fixed loss fraction. The total print volume used in calculating powder usage is denoted in dark green, noting that our model considers the possibility that a portion of the print height will not be used. In this example, $nPartsPerLayer$ is 16, and $nLayersPerBuild$ is 1.

While exemplary values for cost parameters are presented here, we note that the model is intentionally built parametrically and is agnostic to empirical machine performance. For example, build time is derived using the physics-based melt pool scalings described previously, such that a machine- and material-specific build time is calculated for each part geometry. Because the rate model is bounded by the physical limits of the printing process, the cost estimates reflect the fundamental process limits as well.

2.6 Melting history analysis

Toward further application of the rate model to ascertain tradeoffs between throughput and material quality, an analytical solution was also developed to calculate the number of times each point in the build is re-melted, with simplifying assumptions. For the above-mentioned parabolic melt track cross-section profile (i.e. perpendicular to scan direction) and hatch spacing such that two adjacent melt tracks overlap, the integrals of the area bounded by two, one, or zero melt tracks are calculated. Then, for a single layer height interval, the number of intersecting melt tracks is computed, i.e., because within each print layer, the melting history of the prior, current and future material contribute to the melt history of that single layer. For a given unit volume within the print, the proportion of area occupied by the melt tracks horizontally and vertically adjacent are combined to output the proportion of area melted each integer number of times across the depth of the melt track.

Additional assumptions are as follows:

- Laser power, spot size, and scan velocity remain the same for all melt tracks, i.e. this analysis does not account for adapting print strategy and melt pool morphology for different regions of the print (i.e. scanning skin versus core), nor variation in melt track geometry due to varying local temperature of the surrounding tracks/layers.
- Melt tracks can be approximated as perfect parabolic cylinders (i.e. extruded parabolas in space), and therefore balling or lack of fusion are not considered.

Model aspect	**Modelling approach**
Physics-based rate model	
Melt pool shape	Parabolic cross-section, with pre-defined scaling of width and depth
Melt pool depth	Designated as twice the specified layer height
Build orientation	Specified by user, via input CAD file
Print resolution	User-specified layer height set equal to half of laser spot size; laser spot size determined by machine specifications
Hatch spacing	Calculated proportionally to melt track width
Scan strategy	Laser scans perimeter (skin) and area (core) of each contour; area follows a standard zig-zag pattern
Scan speed	Constant and determined by user inputs, machine specifications and rate model; galvanometer precision and laser/mirror dynamics not considered
Nominal build rate	Based on scanning time required to produce 1cc of printed material, with designated spot size, layer thickness, and hatch spacing, excluding recoat time
Activity-based cost model	
Support structures	Increase part mass by a given percentage; support geometry not considered
Packing strategy	Single-layer (in-plane) packing only, by simple division of build area by part bounding box area
Build cycle non-productive time	Machine requires time to warm up and inert, print and cool down for each build
Process gas flow	Required inert gas flow scales with the volume of the build chamber
Recoating time	Per-layer recoating time based on a constant spreading velocity and build plate length
Powder recycling	A fixed fraction of unused powder is recycled
Build plate refurbishment	Build plates can be refurbished a finite number of times
Build plate removal	Assume constant time; costs of labor and machine utilization are applied
Build failure	Captured via uptime assumption
Post-processing	Not considered (i.e., support removal, heat treatment, surface finishing)

Table 2. Summary of modeling approaches for the physics-based rate model and activity-based cost model.

3 RESULTS AND DISCUSSION

3.1 Build rate scaling

Using the rate scaling model described above, we present rate maps for three selected materials in Figure 4, AlSi10Mg, Ti6Al4V, and 1.2709 (maraging) steel. Each map covers a range of laser power (100-1100 W) and spot size (30-150 um), representative of the process parameter space for LPBF. Layer height is equal to half of laser spot size, such that overall print resolution varies in the x-dimension. The color scale (background) shows the volumetric build rate in cc/hr, and the isolines represent normalized enthalpy (dimensionless, red) and laser scan speed (m/s, white). Isolines of build rate are additionally shown in black.

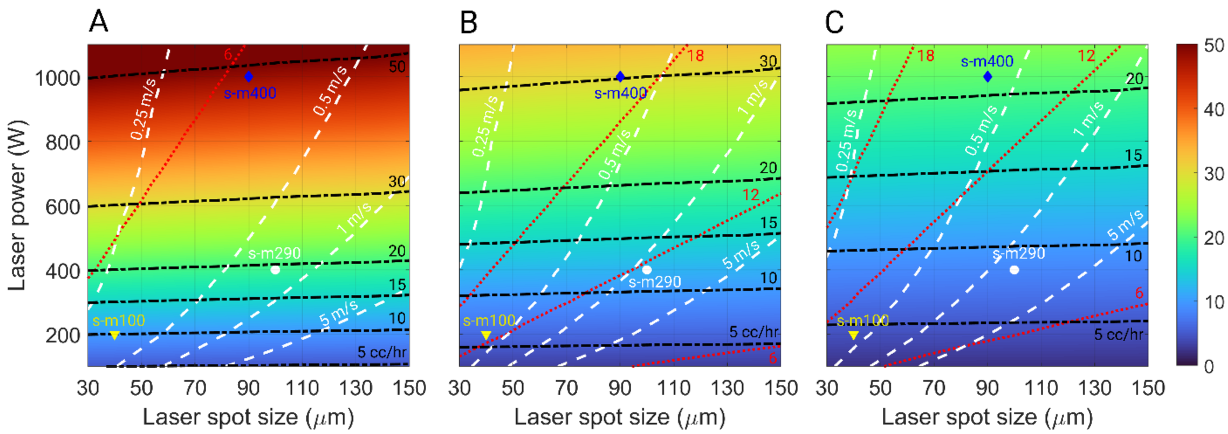

Figure 4. Map of predicted LPBF build rate (cc/hr, in color) as related to laser power and laser spot size for (A) AlSi10Mg, (B) Ti6Al4V, and (C) 1.2709 (maraging) steel. Build rate here is equivalent to total scanning time normalized by part volume. Build rates were calculated by running the complete model (Fig. 1) for a cube geometry (1 cm side length) with layer height set equal to half of laser spot size (note that both layer height and spot size vary proportionally across the x-dimension of each plot). Black lines represent laser scan speed; white lines show normalized enthalpy as a proxy for tendency to produce keyhole pores. All calculations are performed with target melt pool depth equal to 2x layer height and constant ambient temperature of the build chamber and powder at 100 deg C. The predicted operating points corresponding to the maximum laser power and nominal laser spot size for selected commercial LPBF machines (EOS 's-m100', m290, and m400, where 's' denotes simulated), are shown in yellow, white, and blue respectively.

3.1.1 **Interpretation of parameter-rate relationships**

The lower-right area of the P-a space indicates a combination of low power, large laser spot size, and high laser scanning speeds. Lack of fusion would be most likely to occur in this area, whereas the top-left (i.e., high power, small spot size, and slow scanning speeds) would be most likely to produce keyhole-mode defects. As described above, the build rate estimates do not consider these defects, i.e., the rate is calculated for a self-similar parabolic melt pool shape and therefore will have highest accuracy within a stable process parameter window.

Moreover, the overall trends of build rate can be deduced: build rate can vary significantly according to the chosen process parameters, and is systematically higher or lower depending on the material properties that determine the amount of energy required for heating and melting. Build rate is strongly correlated to laser power, more so than spot size. Additionally, for a fixed laser power, as is common in industrial LPBF systems, our model predicts that a low-speed, small-spot size parameter set and a high-power, large-spot size parameter set would produce similar build rates. For LPBF practitioners, these plots could guide the selection of process parameters for a given material and system, such that build rate is maximized while print quality (i.e. avoidance of keyhole pores, lack of fusion defects, etc.) are avoided based on experience or material-specific experiments.

Additionally, we use the rate maps to contextualize the performance of exemplary commercial LPBF equipment. In Figure 4, we place markers representing the nominal maximum laser power and spot size from the data sheets of selected machines from EOS GmbH, and the background color at these points gives the corresponding build rate. The corresponding parameters and output values from the rate model are given in Table 3. Note that the commercial machine models are appended with 'S' (e.g., S-m-100 for the EOS m-100) to indicate that the rate is simulated through model and not measured directly.

Material	**ALSI10MG**			**TI6AL4V**			**1.2709 STEEL**		
Machine	S-m100	S-m290	S-m400	S-m100	S-m290	S-m400	S-m100	S-m290	S-m400
Laser power (W)	200	400	1000	200	400	1000	200	400	1000
Spot size (um)	40	100	90	40	100	90	40	100	90
Layer height (um)	20	50	45	20	50	45	20	50	45
Melt pool depth (um)	40	100	90	40	100	90	40	100	90
Melt pool width (um)	139	349	314	128	320	287	96	240	216
Scan speed (m/s)	2.04	0.65	0.20	1.39	0.44	0.14	1.28	0.41	0.13
Scanning time (hr/cc)	0.10	0.05	0.21	0.16	0.08	0.33	0.23	0.12	0.47
Build rate (cc/hr)	13.92	26.27	66.72	8.68	16.47	41.78	6.08	11.67	29.54
VED	122.8	122.8	122.8	180.4	180.4	180.4	195.6	195.6	195.6

Table 3. Exemplary print parameters for simulated EOS LBPF systems. Data pertains to a 1cc cube. These operating points are shown in Figure 4. Hatch spacing is half of melt track width. Ratio of width to depth is 3.495, 3.195, and 2.405 for AlSi10Mg, Ti6Al4V, and 1.2709 steel, respectively.

3.1.1 **Incorporation of physical build limits**

The transition from conduction to keyhole-mode melting, and the eventual appearance of keyhole pores is typically a main consideration when maximizing LPBF build rate while maintaining low as-built porosity. For 316L stainless steel, King et al. observed that the transition to keyhole mode melt tracks began above a normalized enthalpy value of ~26, and were clearly observed above a normalized enthalpy value of ~34 (King *et al.*, 2014). An additional study characterizing single tracks of 316SS observed that the transition to keyhole mode occurred around a normalized enthalpy value of ~6 (Scipioni Bertoli *et al.*, 2017). Constant normalized enthalpy at values 6, 12 and 18, are reported across the P-a space in Figure 4.

Importantly, we note that normalized enthalpy is material-dependent, i.e. AlSi10Mg's lower enthalpy at melting and melt temperature result in lower normalized enthalpy values compared to Ti6Al4V and 1.709 steel, when process parameters are otherwise identical. This analysis additionally implies that, in the case where some operating points of machines are fixed (e.g., the S-m100, S-m290, and S-m400 each have a fixed spot size regardless of material), the underlying process physics are distinct between materials, and the precise relationships between material properties and energy input must be balanced to ensure high-quality prints.

This analysis also sheds light on the utility of normalized enthalpy as compared to volumetric energy density (VED):

$$VED = \frac{P}{u * H * h}$$

where P is laser power (W), u is scan speed (mm/s), H is hatch spacing (mm) and h is layer thickness (mm). Combining the scaling law between machine parameters, material parameters, and scan speed, and the formulation of VED shows:

$$VED = \frac{\pi H_m \phi}{KA}$$

where H_m is enthalpy at melting, K is an empirical scaling constant (Ye *et al.*, 2019), ϕ is the overmelt parameter (i.e., the ratio between the melt track depth and the print layer height, and A is laser absorptivity. This formulation assumes that the layer thickness h is half of laser spot size a and that the depth of the melt track d is twice the layer thickness h. Each build rate map in Figure 4 has a constant value of VED: 122.8 J/mm3 for AlSi10Mg, 180.4 J/mm3 for Ti6Al4V, and 195.6 J/mm3 for 1.2709 steel. VED is constant across all power-spot size combinations, suggesting that VED alone is insufficient to predict build rate and gain qualitative insights as to the process window according to the normalized enthalpy criterion.

Therefore, while we do not suggest a specific value of normalized enthalpy that bounds the build rate for each specific material, the representation of Figure 4 can be used to select LPBF parameters that may be used to obtain a maximum build rate under a notmalized enthalpy constraint. With this, we show how process limits can be incorporated to threshold the maximum print rate, thus enabling AM process engineers to straightforwardly identify process parameters to increase printing throughput.

3.2 Material- and machine-specific cost dependencies

The parametric rate model, geometry processing pipeline, and process-based cost model can be integrated to provide cost estimates for component manufacturing by LPBF. These cost estimates can be rapidly computed versus material choice, machine capability, process parameters, and other user-defined inputs. As an example, here we compute the cost of a bracket component versus production quantity, LPBF machine selection, and feedstock material (Figure 5). As above, we consider the simulated build rate for a series of commercial machines. Input terms are shown in Tables 1 and 3, as well as the supporting information.

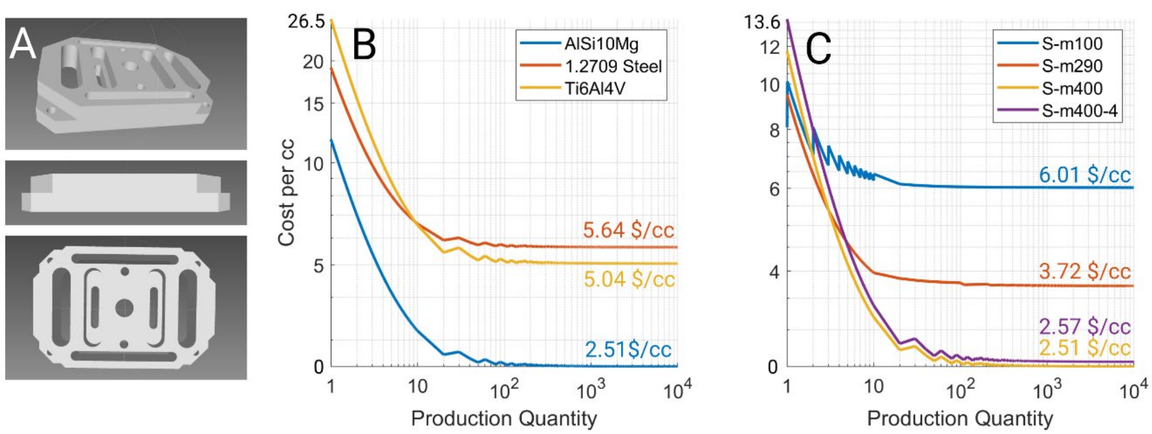

Figure 5. Exemplary output relationships between cost per cc and production quantity. Cost declines with increasing production quantity. **(**A) Bracket geometry in orthogonal, top, and side view. Bounding box of bracket is 7.5cm x 1.25cm x 5cm and the material volume of the bracket is 29.1 cc. (B) Influence of material on production cost per cc using the S-m400 machine. (C) Influence of machine capability (i.e., four emulated EOS LPBF machines) on per-part production cost using AlSi10Mg feedstock.

As shown in Figure 5B, cost per part decreases with production quantity, and becomes constant when the cost of an incremental build is small relative to the total run cost. The observed "sawtoothing" pattern reflects the fact that additional builds become necessary as production quantity increases. Build-specific cost constituents are amortized over the full production volume, such that an additional build will increase the per-cc cost. These increases become less pronounced at high volumes, because the relative contribution of per-build (i.e. variable) costs becomes negligible compared to the contribution of per-part (i.e. fixed) costs under this perspective. For similar reasons, the cost curves appear linear at low production quantities due to the fact that per-part, variable cost is much less than the fixed cost per build. Additionally, these trends are geometry-specific, such that a larger part occupying more of the build chamber would have a different relationship between fixed and variable costs.

Comparing materials, volumetric cost is lowest for AlSi10Mg (2.51 $/cc), second-lowest for Ti6Al4V (5.04 $/cc) and highest for Steel 1.2709 (5.64 $/cc) for the S-m400 at a production quantity of 10,000 (Figure 5B). The difference in cost can be partially explained by the assumed price of raw materials (57, 200, and 50 $ USD/kg for AlSi10Mg, Ti6Al4V and 1.2709 steel, respectively). Additionally, material properties have a large bearing on rate, which in turn has a large bearing on cost: the lower melt temperature and higher specific heat and thermal diffusivity of AlSi10Mg result in a higher build rate and therefore lower cost than the other materials considered here. For high-performance applications, such as lightweighted structures, the selection of feedstock accordingly impacts the ultimate value of the final product as well as its manufacturing cost. Further cost competitiveness could be attained by developing next-generation alloys with lower melting temperatures and more favorable thermal properties.

Figure 5C shows the influence of machine capability on per-part production cost. At low production quantities, smaller machines (S-m100, S-m290) are more cost-effective, although these machines produce fewer components per build at a slower volumetric build rate. The per-build costs, such as build plate usage, inerting gas flow, utilization time for machine warm-up and cool down, are lower for smaller machines due to their smaller build volume. Moreover, the per-hour machine utilization cost for the smaller machines is lower due to lower capital costs.

At high production quantity, however, machine capability dictates cost competitiveness. For example, for AlSi10Mg at $n = 10{,}000$, the cost asymptotes to 6.01 $/cc for the S-m100 and 2.57 $/cc for the S-m400-4, showing the cost advantage of a larger and higher-throughput LPBF machine for component production, despite the significantly higher capital cost. These results indicate that machine capability should be selected to match expected production quantity, and could guide the configuration and allocation of equipment in real-world factory environments.

3.3 Forecasting production cost asymptotes

Additionally, the physics- and process-based approach enables the extrapolation of cost beyond the performance limits of commercially available AM equipment. To date, the main means to increase the throughput of LPBF equipment is to increase the number of independently scanned lasers within the machine, which incurs additional capital cost from the lasers and the required scanning optics and control hardware for each laser, and for coordination of the laser scanning overall. An alternative approach, among others that may emerge, is to provide a single laser beam with much higher power than each laser in the current LPBF machine architecture, and to expose a relatively large area of the powder bed via spatial modulation of the single beam, such as proposed in (Roehling *et al.*, 2021). Ultimately, to gain increased market share, these machines will be reliant upon reducing the capital cost per unit of laser power (i.e., \$/W).

As a limiting thought experiment we query the influence of reducing the power-normalized capital cost (\$/W), by successive orders of magnitude, while assuming no changes to other process costs (Figure 6). This is equivalent to increasing the build rate of an individual machine, without increasing its capital cost, starting from the current economics of LPBF production using the S-m400-4. While artificial, and beyond presently envisioned technology developments, this provides an economic limit to the scaling of LPBF printing cost as machine capability improves.

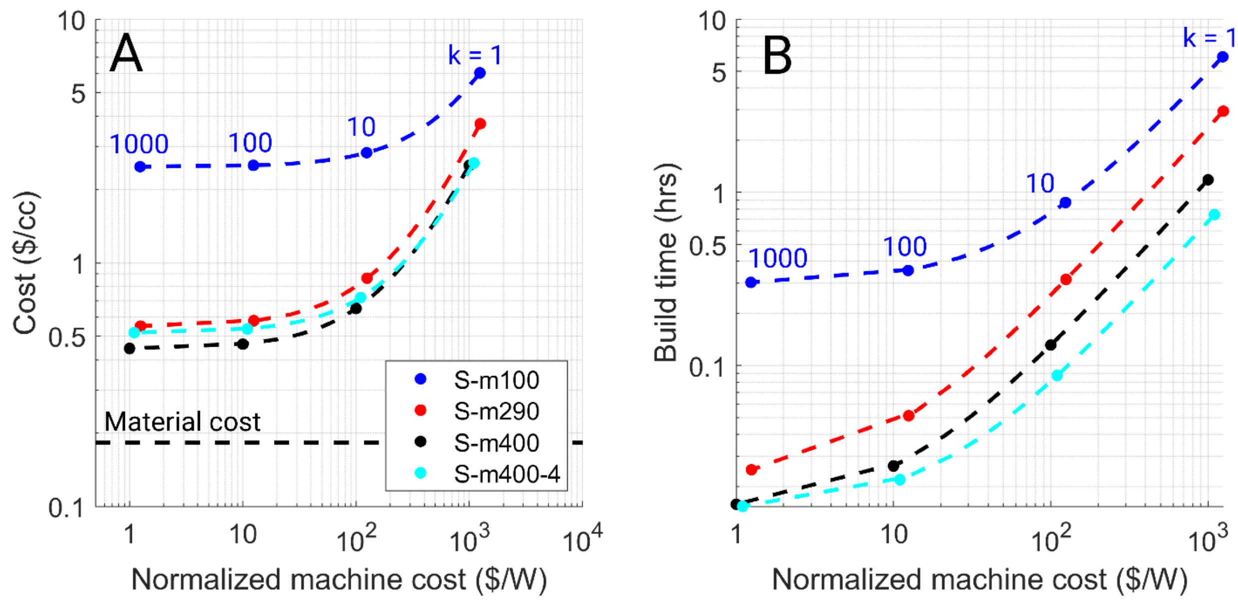

Figure 6. (A) Prospective scaling analysis of the limiting economics of LPBF, via scaling down the machine cost per unit laser power (W) for AlSi10Mg. This analysis is equivalent to assuming that a machine of identical size and capital cost can incorporate additional laser power (and therefore, proportionally, build rate) while maintaining a stable process, We see the asymptotic costs of the LPBF process, relative to material cost. (B) Articulation of the resulting improvement in build time to produce the bracket geometry show in in Fig. 5A. In both (A) and (B) the labels k = 1, 10… indicate the multiple of laser powder that achieves the normalized machine cost (\$/W) indicated on the x-axis.

This analysis is equivalent to assuming that a machine of identical size and capital cost can incorporate additional laser power (and therefore, proportionally, build rate) while maintaining a stable process. We see the asymptotic costs of the LPBF process, relative to material cost, shown here for AlSi10Mg. From this, production cost (i.e. \$/cc) and normalized machine capital cost (i.e. \$/W) are positively, but weakly, correlated (R2 = 0.598, plot not shown). From this analysis, we make two key conclusions: first, the \$/cc asymptotes to a lower-bound as \$/W surpasses

~0.1x that of current technology; second, material cost represents a significant fraction of the asymptotic cost of LPBF. This limiting analysis, while rooted in coarse assumptions and not considerate of other required (and enabling) productivity enhancements (e.g., process automation, increased machine capacity), sheds light on the long-range economics of LPBF. Such analyses are useful for strategic planning, and for drawing comparisons to both conventional metal shaping processes (e.g., machining, casting), and alternative AM processes (e.g., binder jetting) in the future.

3.4 Melting history analysis

While the above analysis is based on the net build rate for both nominal unit volumes of material, and part-specific geometries, the geometric approach by which melt tracks are overlapped in the model enables a bounding analysis of the cyclic thermal history. Here, as described in Section 2.6, we consider the geometric intersection of each consecutive melt track with adjacent tracks both laterally and into the substrate (i.e., the build plate and/or previous layer(s) of solidified material), to provide a lower-bound on the number of times that the material is melted during the LPBF process. Our analysis provides a lower-bound because the model assumes that the material surrounding each melt track returns to the starting temperature, i.e., there is no residual heat build-up. The number of melt cycles is therefore a proxy for the degree of intrinsic, cyclic heat treatment in LPBF, and can be adjusted for a different objective function such as the number of times that each point within the build exceeds a specific transition temperature.

Due to the parabolic melt track geometry, and the assumed rotation of scan pattern from layer to layer, the number of melt cycles is represented by a distribution, which is presented versus the overmelt parameter (phi) in Figure 7C. Increasing phi results in a deeper melt pool, and therefore material is re-melted more times on average. Using this analysis, it becomes feasible to identify parameters that would produce a desired minimum number of melting cycles for each point in the build. A minimum value of $\Phi = 1.34$ (i.e., the melt track depth must extend past the intended layer height by 34%) is required to ensure that all area is melted at least once, here for beta $\beta = \Phi/4$, h = 50 um, w = 200 um. Moreover, to melt all material at least twice, a minimum value of $\Phi = 2.69$ is required, subject to the same parameters, as shown in Figure 7C. Increasing hatch distance results in lower average number of melting cycles, but the effect of increasing hatch is less dramatic than increasing overmelt (Figure 7D). Increasing the number of melting cycles may be desirable for improving microstructure homogeneity or refining microstructure *in situ*, but will also decrease build rate.

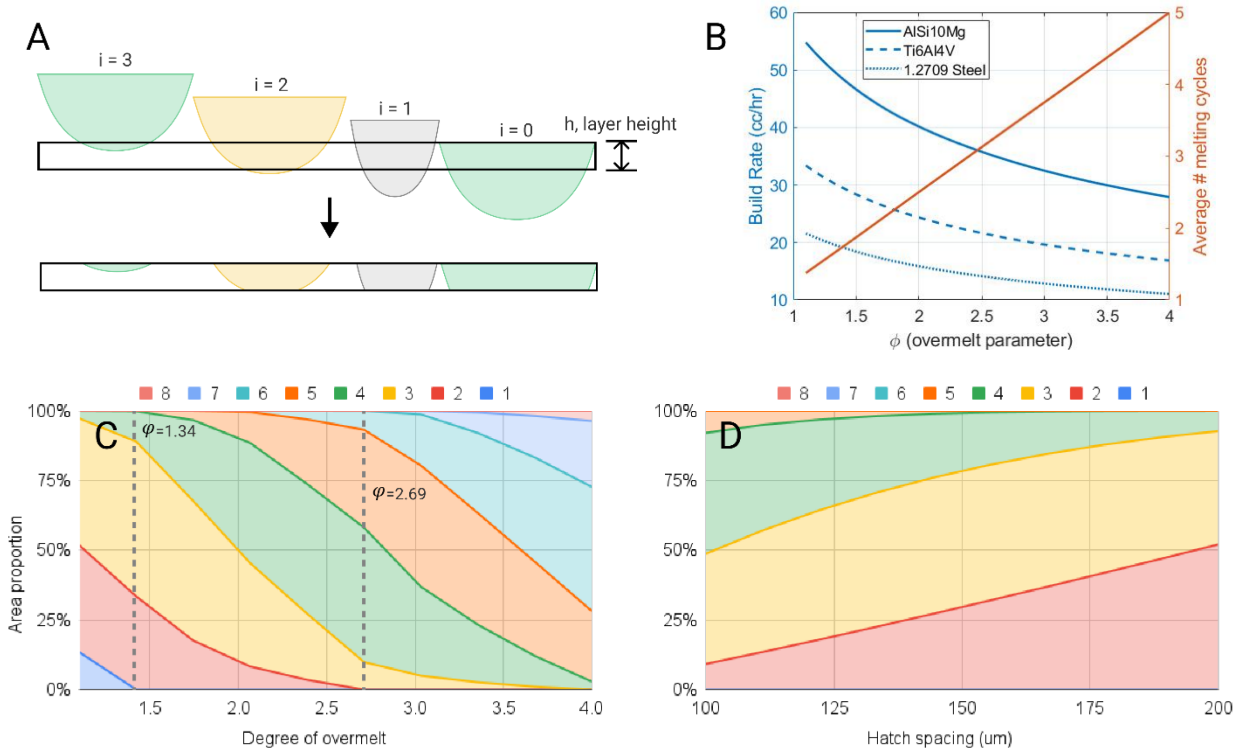

Figure 7. Geometric analysis of overlapping melt tracks in conduction mode LPBF. (A) Decomposition of overlapping melt tracks for a given layer height (i.e., black box). Since each melt track may span multiple layers, the number of times the material within a single layer is re-melted must consider the superposition of all intersecting melt tracks. (B) Tradeoff between build rate and overmelt parameter, which represents the ratio of nominal melt pool depth to layer thickness. Line shows average number of melting-freezing cycles experienced by each point within the build. Values are computed for laser P = 1000W and a = 90m, simulating the specifications of the EOS m400 system. Build rates apply to a simple rectangular prism (5mm x 5mm x 2.5mm). Melt track width is 200 um and layer height is 50um. (C) Influence of overmelt (i.e. vertical overlap between print layers) on distribution of number of melting-freezing cycles. Colors represent the proportion of unit area of the print that was melted once, twice, etc, disregarding edge effects at component surface. (D) Influence of hatch spacing on number of melt cycles.

This analysis relies solely on the geometry of the melt tracks, and therefore these results can be applied to any material subject to these dimensions. However, in practical implementation, the values of h, w, and H may be chosen differently for various materials, and should include the influence of heat retention in adjacent tracks and consecutive layers which would increase the average number of melting cycles under any nominal LPBF parameter set. Nevertheless, this analysis can identify process parameters that guarantee a minimum number of melting cycles at all points throughout a build, and rationalize inhomogeneity in thermal history due to heat flow intrinsic to the LPBF process.

3.5 **Future work**
We see a number of opportunities to build upon the initial capabilities presented here. First, for LPBF, a more accurate estimate of the build rate can be obtained by incorporating (or, validating the scaling model against), more advanced models of melt track scaling. Along with this, the process window (e.g., power, speed, spot size) can be thresholded where undesired instabilities occur, such as balling or keyhole pore formation (Grasso and Colosimo, 2017).

At a system-level, this model can be incorporated in a factory-level simulation that considers the performance of individual machines, along with discrete events such as print jobs, part assignment, and labor allocation (Shakirov *et al.*, 2021). Such a simulation can give a more practical understanding of the operating cost of an AM facility, while remaining informed by part-, process-, and machine-specific details. Including post-processing steps—namely heat treatment, part removal, and support removal, as well as CNC machining in relevant cases (Atia *et al.*, 2017)—will also enrich the utility of the model for AM practitioners across the product lifecycle (Asensio Dominguez *et al.*, 2020; Boschetto *et al.*, 2020).

Last, this framework of physics-driven rate and cost estimation can be translated to other printing processes by substituting the core rate-limiting physical model. For instance, with stereolithography, the model can consider vat photopolymerization of resin instead of powder melting for LPBF, wherein the exothermic polymerization process would impose rate limitations (Walker *et al.*, 2019). Similarly to LPBF, the framework can be further extended to apply a preliminary physical simulation, such as reaction-diffusion or multi-physics process analysis, before geometrical processing to approximate the underlying process physics. Applications of the framework to other AM processes would enable present and future comparisons of economics and industrial viability for production (Westbeek *et al.*, 2020; Wu *et al.*, 2018).

4 Conclusion
In this paper, we present a numerical framework for quantitative analysis of AM cost, in support design exploration and business-oriented decision-making. The framework involves: (1) a build rate estimator that considers the first-order scaling of the process as related to its fundamental parameters, applied to LPBF; and (2) a cost estimator that quantitatively links machine specifications, process parameters and build rate, to cost for LPBF. This model explores the interrelations between cost, throughput, resolution and production quantity for accessible process parameter combinations, namely tradeoffs between throughput (build rate) and resolution, going beyond the fixed operating points that are interpreted from commercial machine data. As such, the rate and cost estimators can be used for screening large libraries of components for AM suitability, and informing equipment design and selection as related to production objectives (e.g., total volume, required lead time, etc). It is our hope that, with the development of parameterized, granularized models of rate, cost, quality and flexibility, we can enable

innovative designers, engineers and production managers to unlock the full benefits of AM and digital manufacturing as a whole.

References

Alexander, P., Allen, S. and Dutta, D. (1998), "Part orientation and build cost determination in layered manufacturing", *Computer-Aided Design*, Elsevier, Vol. 30 No. 5, pp. 343–356.

Artzt, K., Mishurova, T., Bauer, P.P., Gussone, J., Barriobero-Vila, P., Evsevleev, S., Bruno, G., *et al.* (2020), "Pandora's Box–Influence of Contour Parameters on Roughness and Subsurface Residual Stresses in Laser Powder Bed Fusion of Ti-6Al-4V", *Materials 2020, Vol. 13, Page 3348*, Multidisciplinary Digital Publishing Institute, Vol. 13 No. 15, p. 3348.

Asensio Dominguez, L., Xu, F., Shokrani, A., Flynn, J.M., Dhokia, V. and Newman, S.T. (2020), "Guidelines when considering pre & post processing of large metal additive manufactured parts", *Procedia Manufacturing*, Elsevier, Vol. 51, pp. 684–691.

Atia, M., Khalil, J. and Mokhtar, M. (2017), "A COST ESTIMATION MODEL FOR MACHINING OPERATIONS; AN ANN PARAMETRIC APPROACH", *Journal of Al-Azhar University Engineering Sector*, Vol. 12 No. 44, pp. 878–885.

Awad, A., Trenfield, S.J., Goyanes, A., Gaisford, S. and Basit, A.W. (2018), "Reshaping drug development using 3D printing", *Drug Discovery Today*, Elsevier Current Trends, Vol. 23 No. 8, pp. 1547–1555.

Baumers, M., Dickens, P., Tuck, C. and Hague, R. (2016), "The cost of additive manufacturing: machine productivity, economies of scale and technology-push", *Technological Forecasting and Social Change*, North-Holland, Vol. 102, pp. 193–201.

Boschetto, A., Bottini, L., Macera, L. and Veniali, F. (2020), "Post-Processing of Complex SLM Parts by Barrel Finishing", *Applied Sciences 2020, Vol. 10, Page 1382*, Multidisciplinary Digital Publishing Institute, Vol. 10 No. 4, p. 1382.

Chen, C.C. and Sullivan, P.A. (1996), "Predicting total build-time and the resultant cure depth of the 3D stereolithography process", *Rapid Prototyping Journal*, Vol. 2 No. 4, pp. 27–40.

Cheng, L. and To, A. (2019), "Part-scale build orientation optimization for minimizing residual stress and support volume for metal additive manufacturing: Theory and experimental validation", *Computer-Aided Design*, Elsevier, Vol. 113, pp. 1–23.

Choi, S.H. and Samavedam, S. (2002), "Modelling and optimisation of Rapid Prototyping", *Computers in Industry*, Elsevier, Vol. 47 No. 1, pp. 39–53.

Costabile, G., Fera, M., Fruggiero, F., Lambiase, A. and Pham, D. (2017), "Cost models of additive manufacturing: A literature review", *International Journal of Industrial Engineering Computations*, Vol. 8, pp. 263–282.

Cunningham, R., Zhao, C., Parab, N., Kantzos, C., Pauza, J., Fezzaa, K., Sun, T., *et al.* (2019), “Keyhole threshold and morphology in laser melting revealed by ultrahigh-speed x-ray imaging”, *Science*, American Association for the Advancement of Science, Vol. 363 No. 6429, pp. 849–852.

Ding, J., Baumers, M., Clark, E.A. and Wildman, R.D. (2021), “The economics of additive manufacturing: Towards a general cost model including process failure”, *International Journal of Production Economics*, Elsevier, Vol. 237, p. 108087.

Giannatsis, J., Dedoussis, V. and Laios, L. (1999), “Build-Time Estimation Tools for Rapid Prototyping Stereolithography Systems”, pp. 373–384.

“GitHub - JuliaIO/MeshIO.jl: IO for Meshes”. (2019), , available at: https://github.com/JuliaIO/MeshIO.jl (accessed 3 January 2022).

Grasso, M. and Colosimo, B.M. (2017), “Process defects and in situ monitoring methods in metal powder bed fusion: a review”, *Measurement Science and Technology*, IOP Publishing, Vol. 28 No. 4, p. 044005.

Großmann, A., Felger, J., Frölich, T., Gosmann, J. and Mittelstedt, C. (2019), “Melt pool controlled laser powder bed fusion for customised low-density lattice structures”, *Materials and Design*, Elsevier Ltd, Vol. 181, p. 108054.

Gusarov, A. V. and Smurov, I. (2010), “Modeling the interaction of laser radiation with powder bed at selective laser melting”, *Physics Procedia*, Vol. 5 No. PART 2, pp. 381–394.

Hann, D.B., Iammi, J. and Folkes, J. (2011), “A simple methodology for predicting laser-weld properties from material and laser parameters”, *Journal of Physics D: Applied Physics*, IOP Publishing, Vol. 44 No. 44, p. 445401.

Jacobs, P.F. (1993), “Rapid prototyping & manufacturing— Fundamentals of stereolithography”, *Journal of Manufacturing Systems*, Elsevier BV, Vol. 12 No. 5, pp. 430–433.

James, M.S. (2021), “Additive Manufacturing and the U.S. Army’s Improved Turbine Engine | Article | The United States Army”, available at: https://www.army.mil/article/248519/additive_manufacturing_and_the_u_s_armys_improved_turbine_engine (accessed 8 September 2021).

Kechagias, J., Maropoulos, S. and Karagiannis, S. (2004), “Process build-time estimator algorithm for laminated object manufacturing”, *Rapid Prototyping Journal*, Vol. 10 No. 5, pp. 297–304.

King, W.E., Barth, H.D., Castillo, V.M., Gallegos, G.F., Gibbs, J.W., Hahn, D.E., Kamath, C., *et al.* (2014), “Observation of keyhole-mode laser melting in laser powder-bed fusion additive manufacturing”, *Journal of Materials Processing Technology*, Elsevier B.V., Vol. 214 No. 12, pp. 2915–2925.

KOTADIA. (2021), “A review of Laser Powder Bed Fusion Additive Manufacturing of aluminium alloys: Microstructure and properties”, *Additive Manufacturing*, Vol. 46C, pp.

195–225.

Kranz, J., Herzog, D. and Emmelmann, C. (2014), “Design guidelines for laser additive manufacturing of lightweight structures in TiAl6V4”, *Journal of Laser Applications*, Laser Institute of America LIA , Vol. 27 No. S1, p. S14001.

Kruth, J.P., Froyen, L., Van Vaerenbergh, J., Mercelis, P., Rombouts, M. and Lauwers, B. (2004), “Selective laser melting of iron-based powder”, *Journal of Materials Processing Technology*, Elsevier, Vol. 149 No. 1–3, pp. 616–622.

Lindemann, C., Jahnke, U., Moi, M. and Koch, R. (2012), “Analyzing product lifecycle costs for a better understanding of cost drivers in additive manufacturing”, *23rd Annual International Solid Freeform Fabrication Symposium - An Additive Manufacturing Conference, SFF 2012*, pp. 177–188.

Meier, C., Penny, R.W., Zou, Y., Gibbs, J.S. and Hart, A.J. (2018), “Thermophysical Phenomena in Metal Additive Manufacturing By Selective Laser Melting: Fundamentals, Modeling, Simulation, and Experimentation”, *Annual Review of Heat Transfer*, Vol. 20 No. 1, pp. 241–316.

Mukherjee, T., Wei, H.L., De, A. and DebRoy, T. (2018), “Heat and fluid flow in additive manufacturing – Part II: Powder bed fusion of stainless steel, and titanium, nickel and aluminum base alloys”, *Computational Materials Science*, Vol. 150 No. April, pp. 369–380.

Nath, P., Nanda, D., Dinda, G.P. and Sen, I. (2021), “Assessment of Microstructural Evolution and Mechanical Properties of Laser Metal Deposited 316L Stainless Steel”, *Journal of Materials Engineering and Performance 2021*, Springer, pp. 1–11.

Oh, Y., Zhou, C. and Behdad, S. (2018), “Production planning for mass customization in additive manufacturing: Build orientation determination, 2D packing and scheduling”, *Proceedings of the ASME Design Engineering Technical Conference*, American Society of Mechanical Engineers (ASME), Vol. 2A-2018, available at:https://doi.org/10.1115/DETC2018-85639.

Oliveira, J.P., LaLonde, A.D. and Ma, J. (2020), “Processing parameters in laser powder bed fusion metal additive manufacturing”, *Materials & Design*, Elsevier, Vol. 193, p. 108762.

Roehling, J.D., Khairallah, S.A., Shen, Y., Bayramian, A., Boley, C.D., Rubenchik, A.M., DeMuth, J., *et al.* (2021), “Physics of large-area pulsed laser powder bed fusion”, *Additive Manufacturing*, Elsevier, Vol. 46, p. 102186.

Rubenchik, A.M., King, W.E. and Wu, S.S. (2018), “Scaling laws for the additive manufacturing”, *Journal of Materials Processing Technology*, Elsevier, Vol. 257 No. October 2017, pp. 234–243.

Scipioni Bertoli, U., Wolfer, A.J., Matthews, M.J., Delplanque, J.P.R. and Schoenung, J.M. (2017), “On the limitations of Volumetric Energy Density as a design parameter for Selective Laser Melting”, *Materials & Design*, Elsevier, Vol. 113, pp. 331–340.

Shakirov, E., Gee, K., Quinlan, H., Hart, A.J., Fortin, C. and Uzhinsky, I. (2021), "Simulating the AM Production Facility: A Configurable Software Tool for Strategic Facility-Level Planning", *ASME 2020 15th International Manufacturing Science and Engineering Conference, MSEC 2020*, American Society of Mechanical Engineers Digital Collection, Vol. 2, available at:https://doi.org/10.1115/MSEC2020-8308.

Thomas, M., Baxter, G.J. and Todd, I. (2016), "Normalised model-based processing diagrams for additive layer manufacture of engineering alloys", *Acta Materialia*, Elsevier Ltd, Vol. 108, pp. 26–35.

Tofail, S.A.M., Koumoulos, E.P., Bandyopadhyay, A., Bose, S., O'Donoghue, L. and Charitidis, C. (2018), "Additive manufacturing: scientific and technological challenges, market uptake and opportunities", *Materials Today*, Elsevier, Vol. 21 No. 1, pp. 22–37.

Tuck, C.J., Hague, R.J.M., Ruffo, M., Ransley, M. and Adams, P. (2008), "Rapid manufacturing facilitated customization", *Https://Doi.Org/10.1080/09511920701216238*, Taylor & Francis , Vol. 21 No. 3, pp. 245–258.

Walker, D.A., Hedrick, J.L. and Mirkin, C.A. (2019), "Rapid, large-volume, thermally controlled 3D printing using a mobile liquid interface", *Science*, American Association for the Advancement of Science, Vol. 366 No. 6463, pp. 360–364.

Weller, C., Kleer, R. and Piller, F.T. (2015), "Economic implications of 3D printing: Market structure models in light of additive manufacturing revisited", *International Journal of Production Economics*, Elsevier, Vol. 164, pp. 43–56.

Westbeek, S., Remmers, J.J.C., van Dommelen, J.A.W. and Geers, M.G.D. (2020), "Multi-scale process simulation for additive manufacturing through particle filled vat photopolymerization", *Computational Materials Science*, Elsevier, Vol. 180, p. 109647.

Wu, J., Zhao, Z., Hamel, C.M., Mu, X., Kuang, X., Guo, Z. and Qi, H.J. (2018), "Evolution of material properties during free radical photopolymerization", *Journal of the Mechanics and Physics of Solids*, Pergamon, Vol. 112, pp. 25–49.

Yadroitsev, I., Bertrand, P. and Smurov, I. (2007), "Parametric analysis of the selective laser melting process", *Applied Surface Science*, North-Holland, Vol. 253 No. 19, pp. 8064–8069.

Ye, J., Khairallah, S.A., Rubenchik, A.M., Crumb, M.F., Guss, G., Belak, J. and Matthews, M.J. (2019), "Energy Coupling Mechanisms and Scaling Behavior Associated with Laser Powder Bed Fusion Additive Manufacturing", *Advanced Engineering Materials*, John Wiley & Sons, Ltd, Vol. 21 No. 7, pp. 1–9.

Zhang, C. and Chen, T. (2001), "Efficient feature extraction for 2D/3D objects in mesh representation", *IEEE International Conference on Image Processing*, Vol. 3, pp. 935–938.